Nanoscale

Accepted Manuscript

This article can be cited before page numbers have been issued, to do this please use: D. Banerjee, K. J. Sankaran, S. Deshmukh, M. Ficek, C. Yeh, J. Ryl, I. Lin, R. Bogdanowicz, A. Kanjilal, K. Haenen and S. Sinha Roy, *Nanoscale*, 2020, DOI: 10.1039/D0NR00230E.

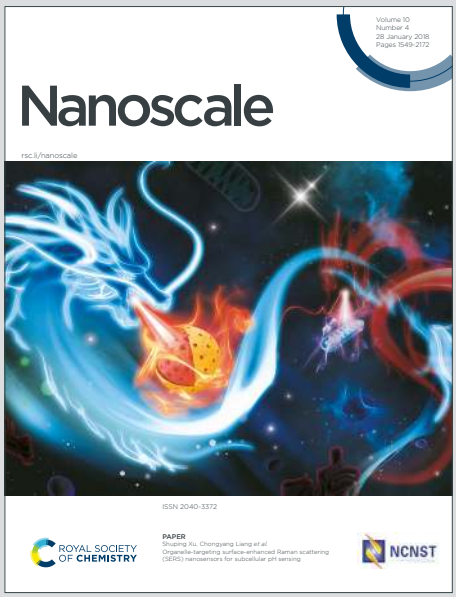

ROYAL SOCIETY OF CHEMISTRY

rsc.li/nanoscale

View Article Online
DOI: 10.1039/D0NR00230E

Single-step grown boron doped nanocrystalline diamond-carbon nanograss hybrid as an efficient supercapacitor electrode

Debosmita Banerjee[a], Kamatchi Jothiramalingam Sankaran[b,c], Sujit Deshmukh[a], Mateusz Ficek,[d] Chien-Jui Yeh[e], Jacek Ryl[f], I-Nan Lin[e], Robert Bogdanowickz[d], Aloke Kanjilal[a], Ken Haenen[b,c], Susanta Sinha Roy[a*]

[a]*Department of Physics, School of Natural Sciences, Shiv Nadar University, NH-91, Gautam Buddha Nagar, Uttar Pradesh 201314, India.*

[b]*Institute for Materials Research (IMO), Hasselt University, 3590 Diepenbeek, Belgium.*

[c]*IMOMEC, IMEC vzw, 3590 Diepenbeek, Belgium.*

[d]*Department of Metrology and Optoelectronics, Faculty of Electronics, Telecommunications and Informatics, Gdansk University of Technology, 11/12 G. Narutowicza St., 80-233 Gdansk, Poland.*

[e]*Department of Physics, Tamkang University, Tamsui, 251 Taiwan, Republic of China.*

[f]*Department of Electrochemistry, Corrosion and Materials Engineering, Faculty of Chemistry, Gdansk University of Technology, Narutowicza 11/12, 80-233 Gdansk, Poland.*

* Corresponding author. Phone: +91-8375955471, E-mail: susanta.roy@snu.edu.in

View Article Online
DOI: 10.1039/D0NR00230E

Abstract

Direct synthesis of nano-structured carbon hybrid consisting of vertically aligned carbon nanograss on top of boron-doped nanocrystalline diamond is demonstrated and the carbon hybrid is further applied as an electrode material for the fabrication of supercapacitor. The hybrid film combines the dual advantages of sp^2 (carbon nanograss) and sp^3 (nanocrystalline diamond) bonded carbon, possessing not only the excellent electrical characteristics of sp^2 carbon but also exceptional electrochemical stability of sp^3 carbon. As a result, the specific capacitance of the as-prepared hybrid material reaches upto 0.4 F cm^{-2}, one of the highest reported in diamond-based supercapacitors. The entire electrochemical results exhibit enhanced electron transfer efficiency with remarkable stability of 95% of capacitance retention even after 10000 cycles.

1. Introduction

Driven by the mandate for miniaturized energy storage systems in portable electronics, digital communications and renewable energy for power grids, the last two decades have seen a tremendous amount of research on the energy storage topic.[1-3] An electrochemical (EC) supercapacitor (SCs) is an energy storage device, offering the best solution in many mainstream energy applications. In EC SCs devices, the energy is stored at the electrode and electrolyte interfaces.[4] Designing a proper electrode material is therefore an important issue for these kinds of EC storage devices. Since the discovery of synthetic nanocarbon allotropes, carbon nanotubes (CNTs), graphene and activated carbon have been regarded as a suitable platform for a plethora of electrochemistry-based applications including energy storage.[5, 6] The foremost advantages of CNTs and graphene-based materials over other commonly used carbonaceous material (glassy carbon and diamond-like carbon) are their unique charge

View Article Online
DOI: 10.1039/D0NR00230E

transport characteristics, combined with their unique low dimensional profile.[7-10] Moreover, attempts have been made to combine graphene and CNTs to prepare electrode materials for rechargeable Li-ion batteries as well as SCs.[10] A significant increase in the energy storage capacity has been observed in this type of hybrids where CNTs are acting as the bridge for rapid electron transfer between the graphene sheets. [11] However, small working potential window in aqueous solution (~1 V) and EC instability especially towards oxidation reaction limits their applicability in energy storage.[12]

Boron doped diamond (BDD), is known for its extreme stability in a wide range of corrosive media like fluoride and alkaline and a boiling mixture of HNO_3 and H_2SO_4.[13] Moreover, a wide potential window even in aqueous solution (~3.2 V) makes BDD very attractive to be used as an electrode material for SCs.[14, 15] Because of these unique physical and EC properties, BDD has fascinated attention worldwide in electrochemical research since 1990s. However, typical BDD has a low surface area, which limits its applicability for EC energy storage.[16] The introduction of high surface area (CNTs or graphene) on BDD is believed to be very promising from the technological point of view. In these hybrid materials, sp^2 carbons (CNTs, graphene) serve the purpose of high charge carrier mobility, high surface area, excellent electrical conductivity and the rich surface chemistry of sp^3 carbon (diamond) provides the desired EC stability. However, experimental fabrication of low dimensional sp^2 carbon on the diamond surface with proper designing of porosity/structure and their orientation is challenging. Up to now, only few successful attempts have been made to integrate sp^2 and sp^3 carbon materials. For example, Nuno *et al.* demonstrated the applicability of diamond-graphite nanoplatelets as an electrochemical sensor.[10] Lee *et al.* showed CNT/BDD core-shell nanowire electrode has a much superior electrochemical performance than that of the lateral BDD electrode.[17] In our previous work, we fabricated vertically aligned BDD-graphene hybrid nanowall electrode for SC application.[18] However,

the synthesis of these hybrids involves multi-step process and time-consuming as well. Therefore a facile single step growth of hybrid structure comprising sp^2 carbon on sp^3-diamond is of a great challenge. In addition, selection of electrolyte is another aspect that also need attention in order to improve the SC performance.

In general, inert electrolytes are commonly employed in carbon-based (activated carbon, graphitized carbon, diamond-like carbon) SC devices for the formation of electrical double-layer capacitors (EDLC) at the electrode-electrolyte interface.[19] Whilst, the introduction of soluble redox species (transition metal ions, halide ions, phenylamide, etc.) into the electrolyte improves the charge storage capacity of any carbon-based SC device.[20, 21] These redox-active species involves in a fast faradaic electron transfer reaction at the electrode-electrolyte interface and such SC is termed as pseudocapacitor.[22] Therefore, apart from the manufacture of proper electrode materials, both inert and redox electrolytes contributions need to be carefully considered.

In this contribution, a unique single-step growth of a boron doped nanocrystalline diamond-carbon nanograss hybrid (we termed it as hybrid carbon nanograss or 'HCNG') using microwave plasma enhanced chemical vapour deposition (MWPECVD) is presented, where the growth conditions varied subsequently during the single synthesis run. Moreover, the plasma was burning continuously during HCNG growth inducing both surface deposition and in-depth structural transformations. Boron doped nanocrystalline diamond (BNCD) and carbon nanograsses (CNGs) are *sp^3 and sp^2* carbon hybrids, where the preferential vertical orientation of *sp^2* bonded CNGs is witnessed on the top of BNCD grains. The suitability of this hybrid electrode in the development of reliable electrochemical SC is demonstrated using both inert electrolyte (1M Na_2SO_4) and redox pair contained electrolyte (1M Na_2SO_4 + 0.05 M Fe $(CN)_6^{3-/4-}$). In addition, in-depth material characterizations (morphological,

View Article Online
DOI: 10.1039/D0NR00230E

microstructural and electrochemical) are carried out to find out the responsible factors for the excellent SC performance.

2. Experimental details

HCNGs were synthesized on silicon substrates by a MWPECVD (2.45 GHz SEKI Technotron AX5400S, Japan) system. Prior to the deposition of these hybrids, the nucleation of the silicon substrates were carried out by a suspension containing nanodiamond particles (BlueSeeds, AdamasNano, USA) and de-ionized water. A gas mixture of $H_2/CH_4/B_2H_6/N_2$ (85%/5%/9%/1%) with a total flow rate of 265 sccm was utilized to grow HCNGs at a microwave power of 1100 W, a process pressure of 35 Torr. The total growth time is 20 h. The substrates were heated to about 650°C using an induction heater and the substrate temperature was measured by a thermocouple. At first 20 min of MWPECVD growth, we applied a negative bias voltage of -200 V to improve the nucleation process of these hybrids. The surface and cross-sectional morphologies were inspected with a scanning electron microscope (SEM; FEI Quanta FEG 250; 10 kV beam accelerating voltage with SE-ETD detector (secondary electron Everhart−Thornley detector) working in a high-vacuum mode (10^{-4} Pa pressure)). The Raman spectrum of the material was recorded within a range of 200–3200 cm^{-1} using a micro-Raman spectrometer (STR) with a 532 nm argon-ion laser. To investigate the surface element compositions and chemical binding properties, high-resolution X-ray photoelectron spectroscopy (XPS) studies were conducted on an Escalab 250 Xi from Thermofisher Scientific with an Al K_α radiation. Pass energy of 20 eV was used for recording the spectra. Compensation of charge was regulated through the low energy Ar^+ ions emission and low-energy electron using a flood gun with emission current, filament current and beam voltage of 150 mA, 3.5 A and 2.1 V respectively. For thorough

understanding, the deconvolution process of the spectra was done with Avantage software (Thermofisher Scientific). A transmission electron microscopy (TEM, Jeol 2100F) and electron energy loss spectroscopy (EELS) in TEM was used to examine the microstructure and the bonding characteristics of this hybrid. The TEM samples were prepared by removing the HCNGs from the Si substrates, followed by ultrasonication in absolute ethanol and coating the TEM grids with a few microliters of the solution.

Electrochemical (EC) measurements including cyclic voltammetry (CV), galvanostatic charge-discharge (GCD), and electrochemical impedance spectroscopy (EIS) of the prepared HCNG electrode material were performed on an Autolab potentiostat-galvanostat PGSTAT302. A standard three electrode cell was employed to inspect the electrochemical performance of the electrodes where the HCNG was used as a working electrode, Ag/AgCl as a reference electrode, and Pt wire as a counter electrode. To execute the EC experiments, two types of electrolytes were used. First an inert aqueous solution of 1M Na_2SO_4 for HCNG electrical double layer capacitors (EDLCs), then a redox-active electrolyte (0.05 M $K_3Fe(CN)_6/K_4Fe(CN)_6$ in 1M Na_2SO_4) was utilized to fabricate HCNG pseudocapacitors (PCs). CVs were performed at different scan rates ranging from 10 – 100 mV s^{-1}. GCD was done at different current densities within the predefined cut off voltage range acquired from CV. The EIS measurements were also conducted with the same electrode-electrolyte arrangement within 0.1 Hz to 100 kHz frequency range. The Nova software (version 1.10) was used to fit the as-recorded Nyquist plots.

3. Results and discussion

Figure 1a shows the cross-sectional SEM micrograph of the HCNGs which reveals the CNGs are grown vertically and randomly all over the BNCD surface, no branching was detected. The tips of the individual grass components are very sharp, with a thickness at the bottom being around 50–100 nm while at the top they become almost point-shaped giving rise to a

View Article Online
DOI: 10.1039/D0NR00230E

grass-like structure. The average height of the nanograss is ~2 μm. The plan-view SEM micrograph in the inset of Figure 1a shows the cauliflower-like grains of the BNCD base. The nanograsses are projecting out of the BNCD films.

In order to examine the different carbonaceous phases present in the hybrid nanostructure, Raman spectroscopy was carried out (Figure 1b). The Raman spectrum of hybrid shows three prominent peaks; the D peak at ~ 1352 cm^{-1}, the first order G peak at ~ 1582 cm^{-1}, and the 2D peak at ~ 2596 cm^{-1}. The D band is forbidden in defect-free graphite structure and its appearance in Raman spectrum is connected with double resonance Raman processes induced by lattice disorder or bent sp^2 carbon bonds, causes in-plane breathing vibrations of the aromatic ring structures (A_{1g} symmetry) while the G band is assigned to the in-plane stretching vibration of sp^2 carbon (E_{2g} symmetry).[23, 24] The less intense Raman structure observed above 2500 cm^{-1} consists of an overtone of D band centered at 2696 cm^{-1} (2D) and a combination of D and G bands (D+G) centered at 2900 cm^{-1}.[25, 26] The broad and low-intensity band around 451 cm^{-1} appears due to boron-induced lattice defects; specifies the existence of boron in the diamond lattice.[27, 28] The peak positions, full width at half maximum and the intensities of D and G bands determined by Lorentzian fitting of Raman spectrum and the fitted parameters are listed in Table S1. The I_D/I_G, and I_{2D}/I_D ratio (Table S1) for the hybrid points to a multiwalled carbon nanotube (MWCNT) like structure,[29, 30] as the top layer on BNCD (cf. Fig. 1(b)).

The chamical bonding and constituents of hybrid structure were futher investigated using XPS and shown in Figure 1c. The primary constituent of the examined samples is *sp²*-carbon, reaching over 60 at.%, analyzed by the peak component located at 284.0 eV (see Figure 1c).[31, 32] The second most notable component observed for the *C1s* spectrum is ascribed to *sp³*-carbon at 284.8 eV. Notably, the *sp²*-to-*sp³* ratio estimated based on XPS peak deconvolution was equal to 2.7:1, which is comparable to the previously obtained results.[31]

The aforementioned structural modification originates from boron and nitrogen incorporation into the nanograss lattice, revealed through the appearance of additional spectral components. The peak at 282.5 eV indicates boron incorporation[32-35] while the peak at 286.6 eV corresponds to C-N bonds, but also C-O interaction makes the exact separation impossible. Finally, the last peak at 289.2 eV should be ascribed to surface carboxyl species.[36] The aforementioned analysis find its confirmation in the *B1s* and *N1s* spectra. The broad peak shape in the *B1s* region (inset (c_1) of Figure 1c)) indicates complex boron interactions within the nanograss lattice. Most notable components are related to elemental boron and B-C bonds (over 1 at.% each),[31, 32, 35, 37, 38] however the contribution at 189.5 eV and 191.0 eV indicates a small presence of B-H and B-O interactions, respectively.[39, 40] Alternatively, the peak revealed in the *N1s* spectrum (inset (c_2) of Figure 1c)) lies in the energy range characteristic for a C-N interaction.[31] Its share however is negligible and does not exceed 0.2 at.%.

TEM was used to examine the microstructure of this hybrid. A bright field TEM (BF-TEM) micrograph (Figure 2a) associated to the BNCD region reveals an acicular nature of carbon nanoclusters, which are uniformly dispersed in the amorphous carbon matrix. The inset of Figure 2a shows the selective area electron diffraction (SAED) pattern of Figure 2a. The SAED contains (111), (220), and (311) diffraction rings of the sp^3-bonded diamond lattice and a bright diffuse ring at the center of the SAED indicates the existence of sp^2-bonded carbon in this hybrid. The Fourier transformed (FT) diffractograms taken from regions 1–3 of high resolution TEM (HRTEM) micrograph (Figure 2b) represent the existence of diamond, graphite and *n*-diamond (*n-D*; an allotrope of diamond)[41, 42] in the BNCD films. The HRTEM micrograph in Figure 2b is corresponding to the region “A” in Figure 2a. Moreover, Figure 2c displays the TEM microstructure of CNGs. The HRTEM micrograph (Figure 2d), corresponding to region “B” in Figure 2c, comprises 5–10 nm sized carbon clusters. The existence of different carbon phases, diamond, *n-D*, and graphite phases,

in the CNGs are revealed by the FT images taken at the regions 4–6, respectively. Furthermore, the carbon K-edge EELS spectrum acquired for HCNGs (Figure 2e) contains a strong σ* contribution at 292 eV and deep valley at 302.0 eV, which signifies the presence of sp^3-bonded carbon.[42] In addition, a core-loss feature in the carbon-K edge at 285 eV (π* band) confirms the existence of graphite.[43, 44] The TEM observations of the HCNGs are in accord with the Raman and XPS studies (cf. Figure 1).

The TEM observations clearly indicate that once the CNGs start forming, the formation of nanodiamond clusters in the materials slowly reduced. This evident that CNGs are originated from the nanographitic clusters contained in the BNCD layer. Hence the formation mechanism of BNCD and CNG is mostly determined by the reactions of the growth plasma and surface induced by the biased voltage. The $CH_4/H_2/B_2H_6/N_2$ plasma used to grow this hybrid mainly contains H^+, C_2, CH, CN, N_2, and BH species, respectively. Basically the C_2 and CH species are responsible for the formation of diamond, graphite and amorphous carbon and the CN and H species are assisting to vary the microstructure of the materials.[45] Once bias is applied, the kinetic energy of these active species increases evidently.[46] As the nanographites are energetically favorable than the nanodiamonds, they form preferentially due to bias.[46-48] The nanodiamond clusters are also formed because of active C_2 species in the plasma. Hence the BNCD layer contains nanodiamond clusters along with the nanographitic phases, which is evident through TEM (cf. Figure 2a). Once the bias is closed, the nanodiamond clusters are not formed due to insufficient kinetic energy of the species and hence the nanographites in BNCD layer help as nuclei for the origin of carbon nanograsses (cf. Figure 2c).

After exploring the structural properties, the HCNG was used as electrode for constructing electrochemical SC. The capacitive behavior was first checked in 1M Na_2SO_4 aqueous solution. The cyclic voltammetry (CV) curves recorded within the potential window

-0.2 V – 1.0 V at different scan rates (Figure 3a) show a symmetrical quasi-rectangular nature representing a practical EDLC type capacitive performance. With increasing scan rate, the capacitive current enhances. The area enclosed under the CV curves provides specific areal capacitance values at different scan rates by using the following equation (1):

$$C_A = \frac{1 \int I(V)dV}{2\Delta V \times \upsilon \times A} \quad \text{----------(1)}$$

Where, ∫I(V)dV is the total current obtained, ΔV is the potential window, υ is the scan rate and A is the geometrical area of the electrode. At the scan rate of 10 mV s^{-1}, the obtained specific capacitance is 0.17 mF cm^{-2}. The variation of specific capacitances with scan rates is shown in Figure S1a.

In the next step, the galvanostatic charge-discharge (GCD) technique was employed to further estimate the capacitance value of the HCNG. The related GCD curves at various current densities from 6 μA cm^{-2} to 20 μA cm^{-2} within the same potential window as obtained from CV are presented in Figure 3b. During charging and discharging, the curves are almost linear and symmetric at higher current densities which demonstrate excellent stable capacitive behavior and very good reversibility of the electrodes. At lower current density (6 μA cm^{-2}), very small nonlinearity was observed, which is due to the charge transfer resistance of the nanostructure and electrolyte interface. The time required for one charge-discharge period decreases with increasing current density. At a current density of 6 μA cm^{-2}, the specific capacitance value calculated from GCD is 0.3 mF cm^{-2}, obtained using the equation (2):

$$C_A = \frac{1\, I \times \Delta t}{2\Delta V \times A} \quad \text{----------(2)}$$

Where I is the capacitive current obtained from GCD, Δt is the charge and discharge time, ΔV is the scanned potential window, and A is the geometric area of the capacitor electrode.

View Article Online
DOI: 10.1039/D0NR00230E

The specific capacitances at different current densities using equation (2) are plotted in Figure S1b.

After examining the EDLC performance, HCNG PCs were constructed by using a redox active electrolyte to further improve the electrochemical activity. In this work, 0.05 M $Fe(CN)_6^{3-/4-}$ was added in 1 M Na_2SO_4 aqueous solution. The related CV measurements (Figure 3c) were done in a potential window of (-0.5) V – 1 V with different scan rates varying from 10 mV s^{-1} to 100 mV s^{-1}. All the curves show a well-defined pair of peaks corresponding to the redox reactions of $Fe(CN)_6^{3-/4-}$. The specific capacitance value evaluated using equation (1) is 0.4 F cm^{-2} at a scan rate of 10 mV s^{-1}. The variation of the obtained capacitance values with scan rate is graphed in Figure S1c.

Associated GCD curves using redox species contained electrolyte with a variation of current density from 3 mA cm^{-2} to 20 mA cm^{-2} in the potential range of -0.5 V to 1 V (as gained from CV) are shown in Figure 3d. A nonlinear characteristic with plateaus was observed for every curve, which indicates the pseudocapacitive behavior of the electrode-electrolyte assembly caused by the redox reactions of $Fe(CN)_6^{3-/4-}$. The specific capacitance at a current density of 3 mA cm^{-2} was found to be 0.25 F cm^{-2} (using equation (2)) and the change of capacitance value with current density is mapped in Figure S1d. It is noticeable that the capacitance values of HCNG PCs with redox active electrolyte obtained from both CV and GCD measurements are almost three fold higher than those of HCNG EDLCs with neutral aqueous solution (the enhancement of capacitance value was from the order of mF cm^{-2} to the order of F cm^{-2}). Such an excellent improvement in the supercapacitor performance is related to the fast and reversible faradaic reactions of the redox pair present in the electrolyte interface which brings an additional pseudocapacitance along with the EDLC contribution. The energy efficiency of HCNG electrodes at current density 3 mA cm^{-2} is found to be 84%. Self-discharge profile of HCNG in redox active electrolyte is shown in

Figure S2 determining the unforced decrease in voltage of charged capacitor in open circuit condition. For this measurement, the system was charged to 1 V at 3 mA cm^{-2} current load and then left open circuited for 100 hours. A sharp voltage drop upto ~0.3 V was observed during the first few minutes (around 8 minutes) of the test followed by a very stable behavior for the rest of the time. The quick drop in voltage signifies the redox active electrolyte based system where the stable linear profile indicates the plateau potential of GCD.[49] After 94 hours, it again started decreasing and after 100 hours the voltage drop was upto 0.25 V only demonstrating a very good self-discharge performance. As a key factor of utilization for practical purposes, the capacitance retention or the cycling stability of HCNGs was examined by charging-discharging at a current density 3 mA cm^{-2} and plotted as a function of cycle number in Figure 4a. After 10000 cycles, an outstanding stability of 95% was observed which evinces an excellent stability of the electrode. Following 10000 cycles of charging-discharging, the surface of the electrode was examined using SEM (inset of Figure 4a), which reveals that there is not much variation in porosity as well as surface morphology of the electrode in comparison to as-grown HCNG shown in Figure 1a. The obtained specific capacitance value was also compared with other carbon based electrodes (listed in table 1) which clearly shows the superior capacitive behavior of the material. Apart from the cycling method, an alternative method known as floating (or voltage holding) test was also performed in 0.05 M $Fe(CN)_6^{-3/-4}$ contained 1 M Na_2SO_4 to imvestigate the long term stability of the electrode.[50] In this method, the electrode is permanently kept at maximum voltage to accelerate the ageing mechanism. For our case, each floating cycle involved several charge-discharge measurements with a current density 3 mA cm^{-2} followed by constant voltage hold at 1 volt (higher voltage side of the potential window obtained from CV and GCD as discussed before) for 2 hours. This process was repeated for 164 hours until 20% loss of capacitance was reached. Figure S3a represents the variation of capacitance retention with

View Article Online
DOI: 10.1039/D0NR00230E

floating time. It is observed that the specific capacitance increases for first 36 hours of floating and then gradually it starts to decrease. After 164 hours, it shows 77.8% of capacitance retention indicating very good stability of the electrode material. The improvement in capacitance retention in first few hours can be explained by more adsorption and intercalation of the electrolyte ions into the internal pores of HGNG electrode.[49, 50] The CV response of the HCNG electrode before and after floating test are shown in Figure S3b. This reflects the irreversible nature of the electrode attributing a little shift of the redox peaks towards higher potential sides and broadening of the peaks after executing the floating test which may be caused due to higher potential attained by the electrode for long time. Another two important capacitive characteristics to define electrochemical performance are energy (E) density and power (P) density; higher the values of these two, better the SC performance. For this study, E density and P density are calculated for three-electrode configuration using the following equations.

$$E = \frac{1}{2} C_A V^2 \quad \text{---------- (3),}$$

$$P = \frac{E}{\Delta t_{dc}} \quad \text{---------- (4)}$$

Where, C_A is the acquired areal specific capacitance, V is scanned potential window as obtained from CV and Δt_{dc} is the discharge time. For HCNGs in redox active electrolyte, Ragone plot connecting areal E density and average P density was plotted in Figure 4b which shows E and P density values ranges from 78.1 μWh cm^{-2} to 17.7 μWh cm^{-2} and 2.8 mW cm^{-2} to 18.7 mW cm^{-2} respectively for current densities varying from 3 mA cm^{-2} to 20 mA cm^{-2}. Figure 4b also summarizes the E and P densities of other diamond structure and silicon nanowire based electrode materials available in literature which illustrates the outstanding energy as well as power delivery of HCNGs in $Fe(CN)_6^{3-/4-}$ contained Na_2SO_4 aqueous electrolyte.[51-55]

View Article Online
DOI: 10.1039/D0NR00230E

Table 1. Comparison of specific capacitance values of HCNG electrodes with other electrode materials in different electrolytes reported in literature.

Capacitor Electrodes	Electrolyte	Capacitance (μF cm^{-2})
Carbon nanotubes[56, 57]	Organic electrolyte	5–9
Graphene[58]	Aqueous	10–40
Graphene[57-59]	Organic electrolyte	4–14
Activated carbon[57]	Aqueous	3–15
Boron doped diamond (BDD)[16]	Na_2SO_4	3.6–7
BDD[60]	$BMIMBF_4$	10.9
Diamond[61]	Tetraethylammonium tetrafluoroborate (Et_4NBF_4)/Propylene carbonate	15.2
N-doped ultrananocrystalline diamond[62]	Phosphate buffered saline (PBS/ NaCl)	17
Silicon nanowires[51, 63]	$PYR_{13}TFSI$, NEt_4BF_4/Propylene carbonate	23–50
Silicon nanotrees[54]	NEt_4BF_4/Propylene carbonate	84
Diamond-coated silicon wire[64]	PMPyrrTFSI/Propylene carbonate	105
N-doped laser induced graphene[65]	Potassium polyacrylate–potassium hydroxide gel	720
3C-SiC/graphene hybrid nanolaminate films[66]	Na_2SO_4 $TBABF_4$ $(Fe(CN)_6^{3-/4-})$+ Na_2SO_4	549.9 297.3 62.2×10^3
Hybrid Carbon Nanowalls[18]	Na_2SO_4	0.43×10^3
Diamond foam[67]	PMPyrrTFSI/PC $NaClO_4$	0.43×10^3 0.5×10^3
Diamond paper[3]	$NaClO_4$	0.6×10^3
Diamond network[68]	$Fe(CN)_6^{3-/4-}$ + Na_2SO_4	73.42×10^3
Carbon nanofiber on boron doped diamond[19]	$Fe(CN)_6^{3-/4-}$ + Na_2SO_4	136.8×10^3
Phosphorus-doped nanocrystalline diamond[69]	Na_2SO_4 $Fe(CN)_6^{3-/4-}$ + Na_2SO_4	11.40 63.56×10^3
HCNGs [This work]	Na_2SO_4 $Fe(CN)_6^{3-/4-}$ + Na_2SO_4	0.3×10^3 400×10^3

View Article Online
DOI: 10.1039/D0NR00230E

Lastly, EIS was performed to understand the electrode kinetics and impedance of the HCNGs. The Nyquist plots acquired in both kind of electrolytes i.e. 1M Na_2SO_4 aqueous solution (Figure 4c) and the redox species containing electrolyte (1 M Na_2SO_4 + 0.05 M $Fe(CN)_6^{3-/4-}$) (inset (I) of Figure 4c)), help to comprehend the conductivity and the ion diffusion of the electrode material. The Nyquist plots show near vertical and linear characteristics in the low frequency region which indicates an ideal capacitive behavior of HCNG electrodes. Little deviation from the utmost ideality can be attributed to the frequency dispersion resulting from the grass-like structure as confirmed by SEM (cf. Figure 1). No distinct semicircular region was seen in the Nyquist plots of the electrode using both kind of electrolytes, which signifies a very low faradaic current.[70, 71]

To analyze the results, an equivalent electrical circuit well-fitted to the Nyquist plot is shown in the inset (II) of Figure 4c. The circuit can be categorized into three separate parts. The first part consist of a series resistance R_s, which describes the solution resistance including the internal resistance of the electrode. The second and third parts of the circuit incorporate charge transfer resistances (R_{CT}) and constant phase elements (CPE). R_{CT} arises due to the rate of redox reactions at the electrode electrolyte interface.[72] CPE is an empirical distributed element, which is a combination of resistance and capacitance and is widely used to describe the non-ideality of the system. The impedance of CPE (Q) can be formulated as $Q=Y_0(j\omega)^{-\alpha}$, where the exponent α is associated with the degree of non-ideality. For α=0, Y_0= R, the component becomes purely resistive, and for α=1, Y_0= 1/C, the component becomes purely capacitive.[73] The second part of the circuit depicts the kinetics of the electrode material. Absence of a well-defined semi-circle indicates a very small charge transfer resistance (R_{CT}) at the electrode/electrolyte interface, because the grass-like structure favours the ion transfer kinetics of the HCNG film. Q_1 emerges from the hybrid nanostructure of HCNG and Q_2 refers to the silicon substrate [18].

View Article Online
DOI: 10.1039/D0NR00230E

Such type of model circuits can also be found in other articles as well.[74, 75] The last portion of the circuit, a parallel link between a charge transfer resistance (R_{CT2}) and Q_3, can be associated with the kinetics of the electrode-electrolyte interface.[76] The goodness of fit (χ^2) for Na_2SO_4 aqueous solution and $Fe(CN)_6^{3-/4-}$ contained Na_2SO_4 is 0.01 and 0.006 respectively that implies excellent fitting.

The fitted circuit parameters are tabulated in Table S2. The series resistance of the HCNG electrode dipped in 1M Na_2SO_4 aqueous electrolyte was ~69 Ω, which was dropped to 10 Ω when 1 M Na_2SO_4 + 0.05 M $Fe(CN)_6^{3-/4-}$ was used as electrolyte. The charge transfer resistance (R_{CT1}) of the neutral aqueous solution was found to be 100 Ω, but an almost 5-fold substantial decrement in R_{CT1} value (~27.9 Ω) in redox species contained Na_2SO_4 solution leads to the fact that the improved performance of HCNGs in redox species active electrolyte can be attributed to both carbon nanograss decorated BNCD and the inclusion of pseudocapacitance by redox active species in the electrolyte. This sort of electrolyte additionally helps to reduce the charge transfer resistance (R_{CT2}) at the electrode-electrolyte interface (~50 Ω), compared to the neutral aqueous electrolyte.

Thus, the enhanced SC performance of the HCNG electrodes can be associated with the presence diamond nanograss which provides large specific surface area and improved charge transfer kinetics while BNCD base facilitates electrochemical stability. However, we believe that the SC performance of HCNG electrodes can further be improved by surface treatment and introducing dopants like nitrogen, phosphorous etc.

4. Conclusions

Boron doped nanocrystalline diamond-carbon nanograss hybrids i.e. HCNGs have been synthesized by the microwave plasma-enhanced chemical vapor deposition technique and further utilized for supercapacitor applications. The HCNG electrode manifests excellent

View Article Online
DOI: 10.1039/D0NR00230E

capacitance value along with noteworthy capacitance retention. Its electrochemical performance in both aqueous and redox active electrolyte has been assessed and supported by CV, GCD and EIS. A much higher capacitance value was obtained with HCNG PCs with redox active solution compared to HCNG EDLCs with inert aqueous solution. Such clever implementation can be accredited to the unique one-dimensional grass-like geometry of CNGs and improved electrical conductivity due to the co-formation of nanographite and diamond phases in BNCD. As a consequence, these generate an enhanced interphase/interfacial physicochemical dynamics. Therefore, for future energy storage systems, the study would pave a broader research aspect of such new hybrid diamond materials.

Conflicts of interest

There are no conflicts to declare.

Acknowledgements

The authors gratefully acknowledge financial support from the Hasselt University Special Research Fund (BOF), the Research Foundation – Flanders (FWO), and the Methusalem NANO network.

References

1. J. R. Miller and P. Simon, *Science*, 2008, **321**, 651.
2. R. Kötz and M. Carlen, *Electrochim. Acta*, 2000, **45**, 2483-2498.
3. F. Gao and C. E. Nebel, *ACS Appl. Mater. Interfaces*, 2016, **8**, 28244-28254.
4. P. Simon and Y. Gogotsi, *Nat. Mater.*, 2008, **7**, 845-854.
5. Y. Zhai, Y. Dou, D. Zhao, P. F. Fulvio, R. T. Mayes and S. Dai, *Adv. Mater.*, 2011, **23**, 4828-4850.
6. A. Hirsch, *Nat. Mater.*, 2010, **9**, 868-871.

7. S. Daniel, T. P. Rao, K. S. Rao, S. U. Rani, G. R. K. Naidu, H.-Y. Lee and T. Kawai, *Sens. Actuators B: Chem.*, 2007, **122**, 672-682.

8. T. W. Prow, J. E. Grice, L. L. Lin, R. Faye, M. Butler, W. Becker, E. M. Wurm, C. Yoong, T. A. Robertson and H. P. Soyer, *Adv. Drug Deliv. Rev.*, 2011, **63**, 470-491.

9. Y. Shao, J. Wang, H. Wu, J. Liu, I. A. Aksay and Y. Lin, *Electroanalysis*, 2010, **22**, 1027-1036.

10. N. F. Santos, S. O. Pereira, A. J. S. Fernandes, T. L. Vasconcelos, C. M. Fung, B. S. Archanjo, C. A. Achete, S. R. Teixeira, R. F. Silva and F. M. Costa, *ACS Appl. Mater. Interfaces*, 2019, **11**, 8470-8482.

11. Z. Fan, J. Yan, L. Zhi, Q. Zhang, T. Wei, J. Feng, M. Zhang, W. Qian and F. Wei, *Adv. Mater.*, 2010, **22**, 3723-3728.

12. G. Wang, L. Zhang and J. Zhang, *Chem. Soc. Rev.*, 2012, **41**, 797-828.

13. R. Hoffmann, A. Kriele, H. Obloh, J. Hees, M. Wolfer, W. Smirnov, N. Yang and C. E. Nebel, *Appl. Phys. Lett.*, 2010, **97**, 052103.

14. N. Yang, J. S. Foord and X. Jiang, *Carbon*, 2016, **99**, 90-110.

15. K. Siuzdak and R. Bogdanowicz, *Energy Technol.*, 2018, **6**, 223-237.

16. S. Yu, N. Yang, H. Zhuang, J. Meyer, S. Mandal, O. A. Williams, I. Lilge, H. Schönherr and X. Jiang, *The J. Phys. Chem. C*, 2015, **119**, 18918-18926.

17. S.-K. Lee, M.-J. Song, J.-H. Kim, T.-S. Kan, Y.-K. Lim, J.-P. Ahn and D.-S. Lim, *NPG Asia Mater.*, 2014, **6**, e115-e115.

18. D. Banerjee, K. J. Sankaran, S. Deshmukh, M. Ficek, G. Bhattacharya, J. Ryl, D. M. Phase, M. Gupta, R. Bogdanowicz and I.-N. Lin, *The J. Phys. Chem. C*, 2019.

19. S. Yu, N. Yang, M. Vogel, S. Mandal, O. A. Williams, S. Jiang, H. Schönherr, B. Yang and X. Jiang, *Adv. Energy Mater.*, 2018, **8**, 1702947.

20. N. Ma, N. Phattharasupakun, J. Wutthiprom, C. Tanggarnjanavalukul, P. Wuanprakhon, P. Kidkhunthod and M. Sawangphruk, *Electrochim. Acta*, 2018, **271**, 110-119.

21. N. Ma, S. Kosasang, N. Phattharasupakun and M. Sawangphruk, *J. Electrochem. Soc.*, 2019, **166**, A695-A703.

22. B. Akinwolemiwa, C. Peng and G. Z. Chen, *J. Electrochem. Soc.*, 2015, **162**, A5054-A5059.

23. A. Baranov, A. Bekhterev, Y. S. Bobovich and V. Petrov, *Opt. Spektrosk.*, 1987, **62**, 99.

24. C. Thomsen and S. Reich, *Phys. Rev. Lett.*, 2000, **85**, 5214.

25. A. C. Ferrari and D. M. Basko, *Nature Nanotech.*., 2013, **8**, 235.

26. M. Pimenta, G. Dresselhaus, M. S. Dresselhaus, L. Cancado, A. Jorio and R. Saito, *Phys. Chem. Chem. Phys.*, 2007, **9**, 1276-1290.

27. P. May, W. Ludlow, M. Hannaway, P. Heard, J. Smith and K. Rosser, *Diamond Relat. Mater.*, 2008, **17**, 105-117.

28. R. Zhang, S. T. Lee and Y. Lam, *Diamond Relat. Mater.*, 1996, **5**, 1288-1294.

29. V. L. Kuznetsov, S. N. Bokova-Sirosh, S. I. Moseenkov, A. V. Ishchenko, D. V. Krasnikov, M. A. Kazakova, A. I. Romanenko, E. N. Tkachev and E. D. Obraztsova, *physica status solidi (b)*, 2014, **251**, 2444-2450.

30. R. A. DiLeo, B. J. Landi and R. P. Raffaelle, *J. Appl. Phys.*, 2007, **101**, 064307.

31. K. Siuzdak, M. Ficek, M. Sobaszek, J. Ryl, M. Gnyba, P. Niedziałkowski, N. Malinowska, J. Karczewski and R. Bogdanowicz, *ACS Appl. Mater. Interfaces*, 2017, **9**, 12982-12992.

32. M. Sobaszek, K. Siuzdak, J. Ryl, M. Sawczak, S. Gupta, S. B. Carrizosa, M. Ficek, B. Dec, K. Darowicki and R. Bogdanowicz, *The J. Phys. Chem. C*, 2017, **121**, 20821-20833.

33. Y. Sun, Q. Meng, M. Qian, B. Liu, K. Gao, Y. Ma, M. Wen and W. Zheng, *Sci. Rep.*, 2016, **6**, 20198.

34. S. Wan, Y. Yu, J. Pu and Z. Lu, *RSC Adv.*, 2015, **5**, 19236-19240.

35. M. K. Kolel-Veetil, R. M. Gamache, N. Bernstein, R. Goswami, S. B. Qadri, K. P. Fears, J. B. Miller, E. R. Glaser and T. M. Keller, *J. Mater. Chem. C*, 2015, **3**, 11705-11716.

36. J. Ryl, L. Burczyk, R. Bogdanowicz, M. Sobaszek and K. Darowicki, *Carbon*, 2016, **96**, 1093-1105.

37. F. L. Pasquale, Y. Li, J. Du and J. A. Kelber, *Journal of Physics: Condens. Matter*, 2013, **25**, 105801.

38. H. Jung, K. Nam, H.-G. Sung, H. Hyun, Y. Sohn and W. Shin, *Materials*, 2016, **9**, 1012.

39. M. Sankaran and B. Viswanathan, *Carbon*, 2007, **45**, 1628-1635.

40. W. Cermignani, T. E. Paulson, C. Onneby and C. G. Pantano, *Carbon*, 1995, **33**, 367-374.

41. H. Hirai and K.-I. Kondo, *Science*, 1991, **253**, 772.

42. P. Kovarik, E. B. D. Bourdon and R. H. Prince, *Phys. Rev. B*, 1993, **48**, 12123-12129.

43. S. Prawer, J. L. Peng, J. O. Orwa, J. C. McCallum, D. N. Jamieson and L. A. Bursill, *Phys. Rev. B*, 2000, **62**, R16360-R16363.

44. J. Kurian, K. J. Sankaran, J. P. Thomas, N. H. Tai, H.-C. Chen and I. N. Lin, *J. Phys. D: Appl. Phys.*, 2014, **47**, 415303.

45. K. J. Sankaran, N. Kumar, J. Kurian, R. Ramadoss, H.-C. Chen, S. Dash, A. K. Tyagi, C.-Y. Lee, N.-H. Tai and I. N. Lin, *ACS Appl. Mater. Interfaces*, 2013, **5**, 3614-3624.

46. K. J. Sankaran, B.-R. Huang, A. Saravanan, D. Manoharan, N.-H. Tai and I. N. Lin, *Plasma Processes and Polym.*, 2016, **13**, 419-428.

47. A. Saravanan, B.-R. Huang, D. Manoharan and I. N. Lin, *ACS Appl. Mater. Interfaces*, 2017, **9**, 4916-4925.

48. A. Saravanan, B.-R. Huang, K. J. Sankaran, S. Kunuku, C.-L. Dong, K.-C. Leou, N.-H. Tai and I. N. Lin, *ACS Appl. Mater. Interfaces*, 2014, **6**, 10566-10575.

49. J. Menzel, E. Frackowiak and K. Fic, *J. Power Sources*, 2019, **414**, 183-191.

50. F. Ochai-Ejeh, D. Y. Momodu, M. Madito, A. A. Khaleed, K. O. Oyedotun, S. Ray and N. Manyala, *AIP Adv.*, 2018, **8**, 055208.

51. D. Aradilla, P. Gentile, G. Bidan, V. Ruiz, P. Gómez-Romero, T. J. S. Schubert, H. Sahin, E. Frackowiak and S. Sadki, *Nano Energy*, 2014, **9**, 273-281.

52. G. S. Gund, D. P. Dubal, D. Aradilla, W. Mueller-Sebert, G. Bidan, D. Gaboriau, P. Gentile, T. J. S. Schubert, J. Wimberg, S. Sadki and P. Gomez-Romero, 2015, International Conference on Industrial Instrumentation and Control (ICIC), pp. 1125-1128.

53. E. Scorsone, N. Gattout, L. Rousseau and G. Lissorgues, *Diamond Relat. Mater.*, 2017, **76**, 31-37.

54. F. Thissandier, P. Gentile, T. Brousse, G. Bidan and S. Sadki, *J. Power Sources*, 2014, **269**, 740-746.

55. L. Gu, Y. Wang, Y. Fang, R. Lu and J. Sha, *J. Power Sources*, 2013, **243**, 648-653.

56. C. Portet, G. Yushin and Y. Gogotsi, *Carbon*, 2007, **45**, 2511-2518.

57. W. Gu and G. Yushin, *WIREs Energy and Environment*, 2014, **3**, 424-473.

58. M. D. Stoller, S. Park, Y. Zhu, J. An and R. S. Ruoff, *Nano Lett.*, 2008, **8**, 3498-3502.

59. Y. Zhu, S. Murali, M. D. Stoller, K. J. Ganesh, W. Cai, P. J. Ferreira, A. Pirkle, R. M. Wallace, K. A. Cychosz, M. Thommes, D. Su, E. A. Stach and R. S. Ruoff, *Science*, 2011, **332**, 1537.

60. D. Y. Kim, J. C. Yang, H. W. Kim and G. M. Swain, *Electrochim. Acta*, 2013, **94**, 49-56.

61. M. Yoshimura, K. Honda, T. Kondo, R. Uchikado, Y. Einaga, T. N. Rao, D. A. Tryk and A. Fujishima, *Diamond Relat. Mater.*, 2002, **11**, 67-74.

62. W. Tong, K. Fox, A. Zamani, A. M. Turnley, K. Ganesan, A. Ahnood, R. Cicione, H. Meffin, S. Prawer, A. Stacey and D. J. Garrett, *Biomaterials*, 2016, **104**, 32-42.

63. F. Thissandier, A. Le Comte, O. Crosnier, P. Gentile, G. Bidan, E. Hadji, T. Brousse and S. Sadki, *Electrochem. Comm.*, 2012, **25**, 109-111.

64. F. Gao, G. Lewes-Malandrakis, M. T. Wolfer, W. Müller-Sebert, P. Gentile, D. Aradilla, T. Schubert and C. E. Nebel, *Diamond Relat. Mater.*, 2015, **51**, 1-6.

65. W. Song, J. Zhu, B. Gan, S. Zhao, H. Wang, C. Li and J. Wang, *Small*, 2018, **14**, 1702249.

66. S. Heuser, N. Yang, F. Hof, A. Schulte, H. Schönherr and X. Jiang, *Small*, 2018, **14**, 1801857.

67. F. Gao, M. T. Wolfer and C. E. Nebel, *Carbon*, 2014, **80**, 833-840.

68. S. Yu, N. Yang, H. Zhuang, S. Mandal, O. A. Williams, B. Yang, N. Huang and X. Jiang, *J. Mater. Chem. A*, 2017, **5**, 1778-1785.

69. S. Yu, J. Xu, H. Kato, N. Yang, A. Schulte, H. Schönherr and X. Jiang, *ChemElectroChem*, 2019, **6**, 1088-1093.

70. Q. Wu, Y. Xu, Z. Yao, A. Liu and G. Shi, *ACS Nano*, 2010, **4**, 1963-1970.

71. T. Purkait, G. Singh, D. Kumar, M. Singh and R. S. Dey, *Sci. Rep.*, 2018, **8**, 640.

72. W. Wang, S. Guo, I. Lee, K. Ahmed, J. Zhong, Z. Favors, F. Zaera, M. Ozkan and C. S. Ozkan, *Sci. Rep.*, 2014, **4**, 4452.

73. H.-K. Song, H.-Y. Hwang, K.-H. Lee and L. H. Dao, *Electrochim. Acta*, 2000, **45**, 2241-2257.

74. H.-B. Choe, H.-S. Lee, M. A. Ismail and M. W. Hussin, *Int. J. Electrochem. Sci.*, 2015, **10**, 9775-9789.

75. D. P. Dubal, S. H. Lee, J. G. Kim, W. B. Kim and C. D. Lokhande, *J. Mater. Chem.*, 2012, **22**, 3044-3052.

76. N. Wei, Y. Jiang, Y. Ying, X. Guo, Y. Wu, Y. Wen and H. Yang, *RSC Adv.*, 2017, **7**, 11528-11536.

View Article Online
DOI: 10.1039/D0NR00230E

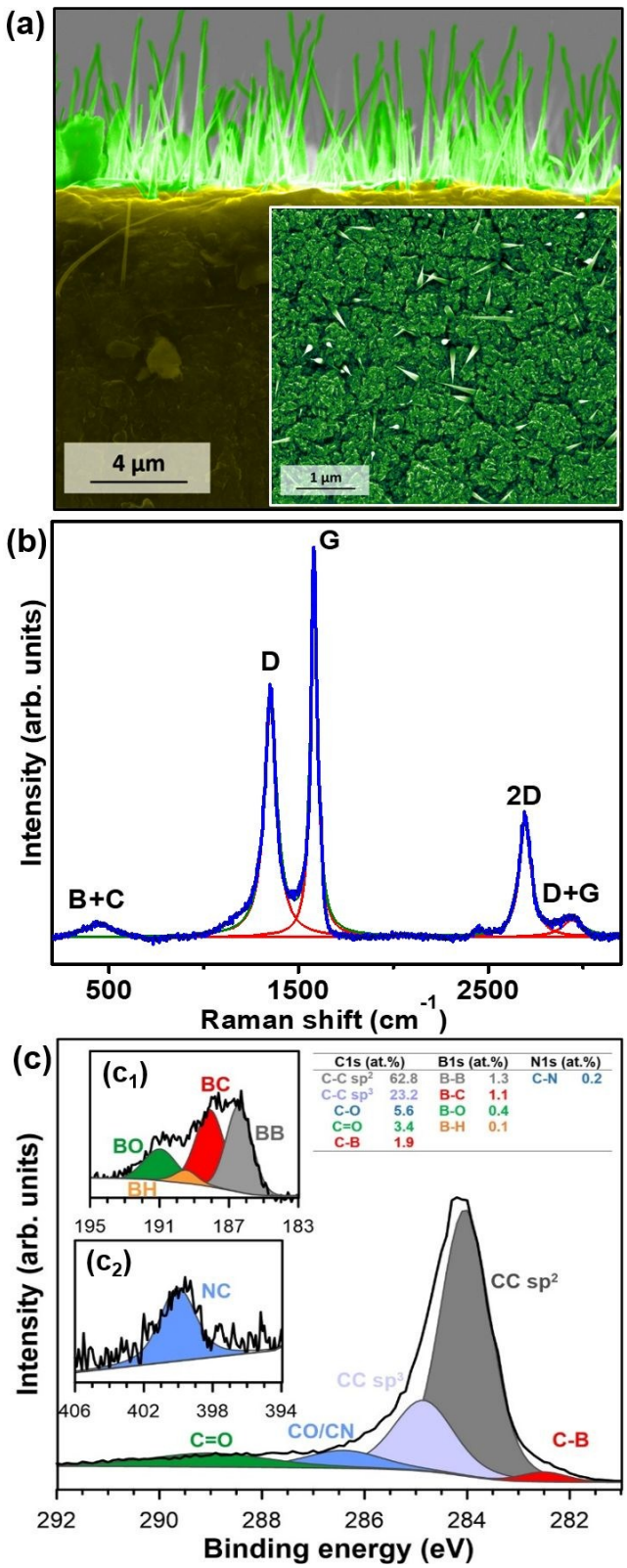

Figure 1. (a) The cross-sectional SEM micrographs of HCNG hybrid, corresponding plan-view image is shown in the inset. (b) Raman spectrum of HCNG hybrid. (c) *C1s* XPS

View Article Online
DOI: 10.1039/D0NR00230E

spectrum of HCNG hybrid along with *B1s* (inset "c_1") and *N1s* (inset "c_2") XPS spectra of the material.

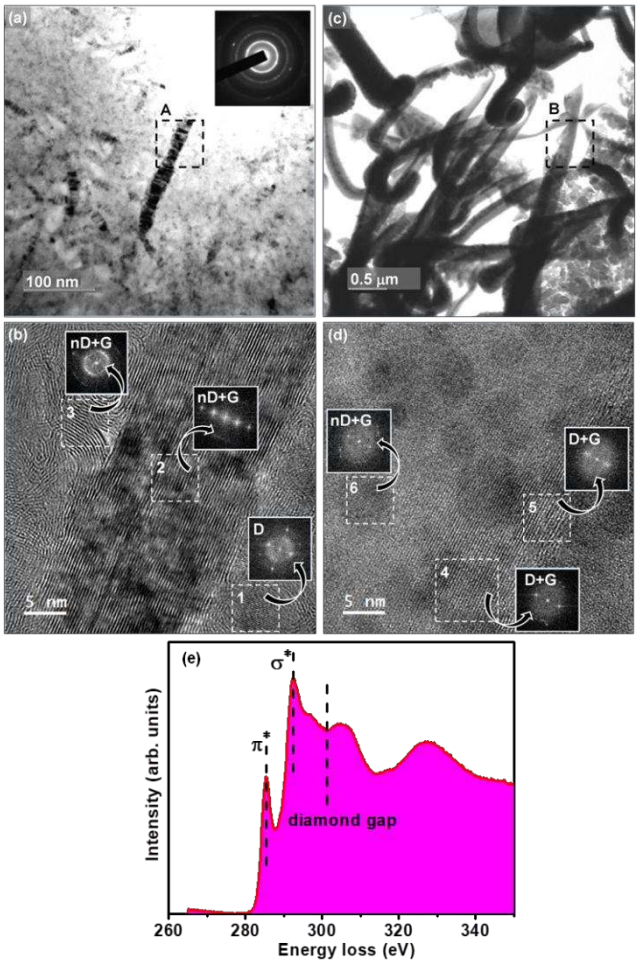

Figure 2. (a) The BF-TEM micrograph of the BNCD region of the HCNG hybrid, whereas the corresponding SAED pattern is shown as inset. (b) A HRTEM micrograph corresponding to the region "A" designated in (a). (c) The BF-TEM micrograph of the CNG region of the HCNG hybrid. (d) A HRTEM micrograph corresponding to the region "B" designated in (c). The Fourier transformed (FT) diffractogram images corresponding to the regions "1–6" of the structure images (b and d) show the existence of diamond, *n*-diamond and graphite phases in the HCNG hybrid, respectively. (e) Carbon K-edge core-loss EELS spectrum of HCNG hybrid.

View Article Online
DOI: 10.1039/D0NR00230E

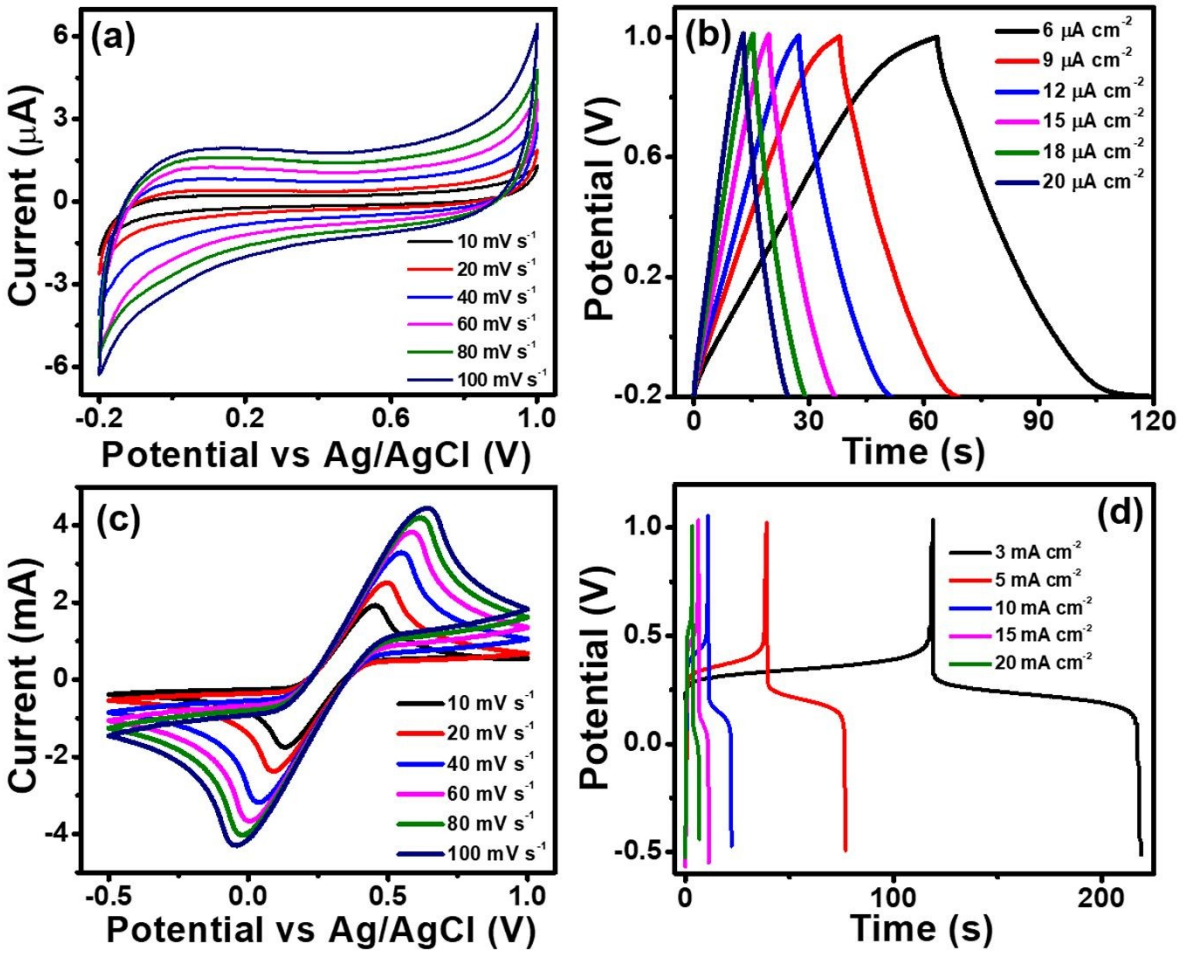

Figure 3. Supercapacitor performance of HCNG electrodes: (a) Cyclic voltammograms at scan rates varying from 10 to 100 mV s^{-1} and (b) galvanostatic charge-discharge curves at current densities from 6 to 20 μA cm^{-2} in 1 M Na_2SO_4 aqueous solution. (c) Cyclic voltammograms at scan rates varying from 10 tp 100 mV s^{-1} and (d) galvanostatic charge-discharge curves at current densities from 3 to 20 mA cm^{-2} in redox active electrolyte of 0.05 M $Fe(CN)_6^{-3/-4}$ contained 1 M Na_2SO_4 aqueous solution.

View Article Online
DOI: 10.1039/D0NR00230E

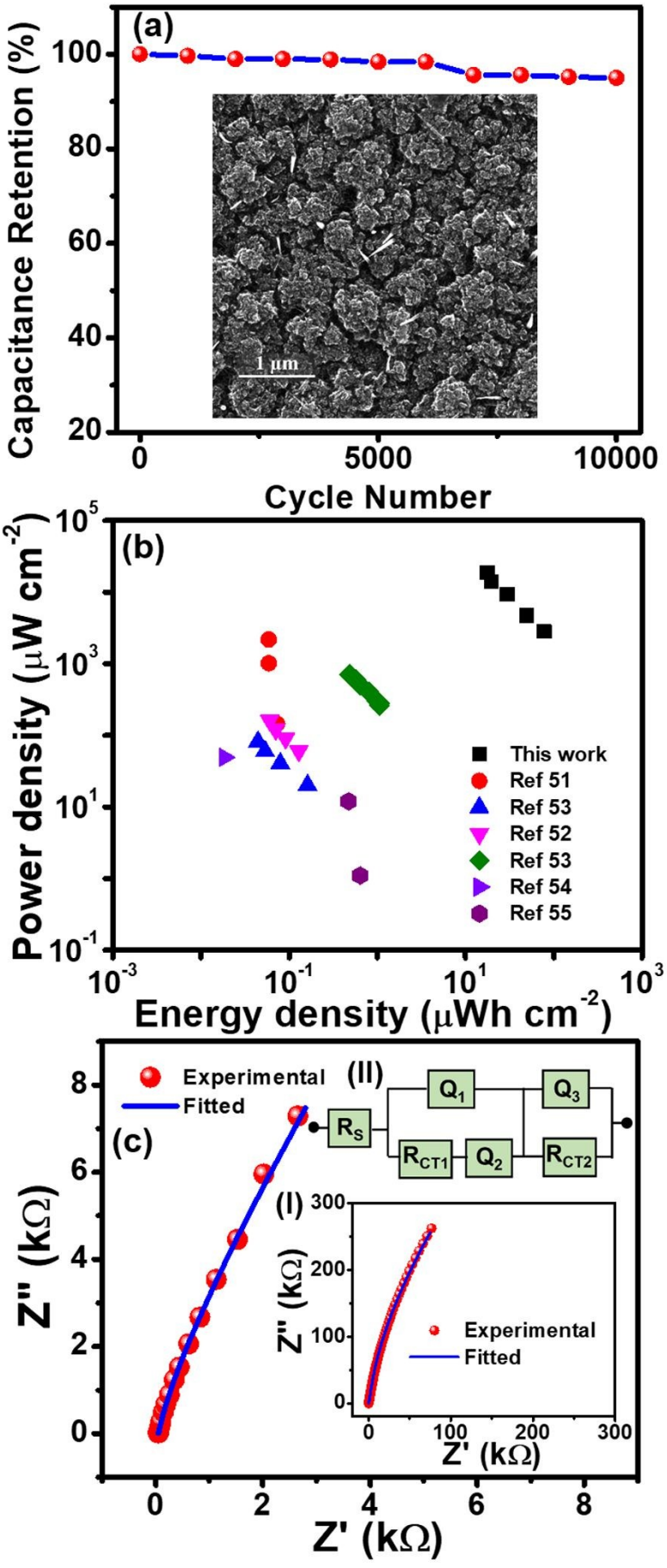

Figure 4. (a) Percentage of capacitance retention as a function of charging-discharging cycle number at 3 mA cm^{-2} current density in redox active electrolyte. Inset shows the SEM image of the HCNG electrode after 10000 cycles of charging-discharging (b) Ragone plot of areal energy density vs. avarage power density of HCNG and other electrodes obtained from literature (c) Experimental and fitted impedance spectra for HCNGs in 0.05 M $Fe(CN)_6^{-3/-4}$ contained 1 M Na_2SO_4 aqueous solution. Inset (I) shows the impedance spectra of HCNGs in neutral 1 M Na_2SO_4 solution and inset (II) shows the equivalent electrical circuit model for both the neutral and redox active electrolytes.

Table of Contents Graphic

View Article Online
DOI: 10.1039/D0NR00230E

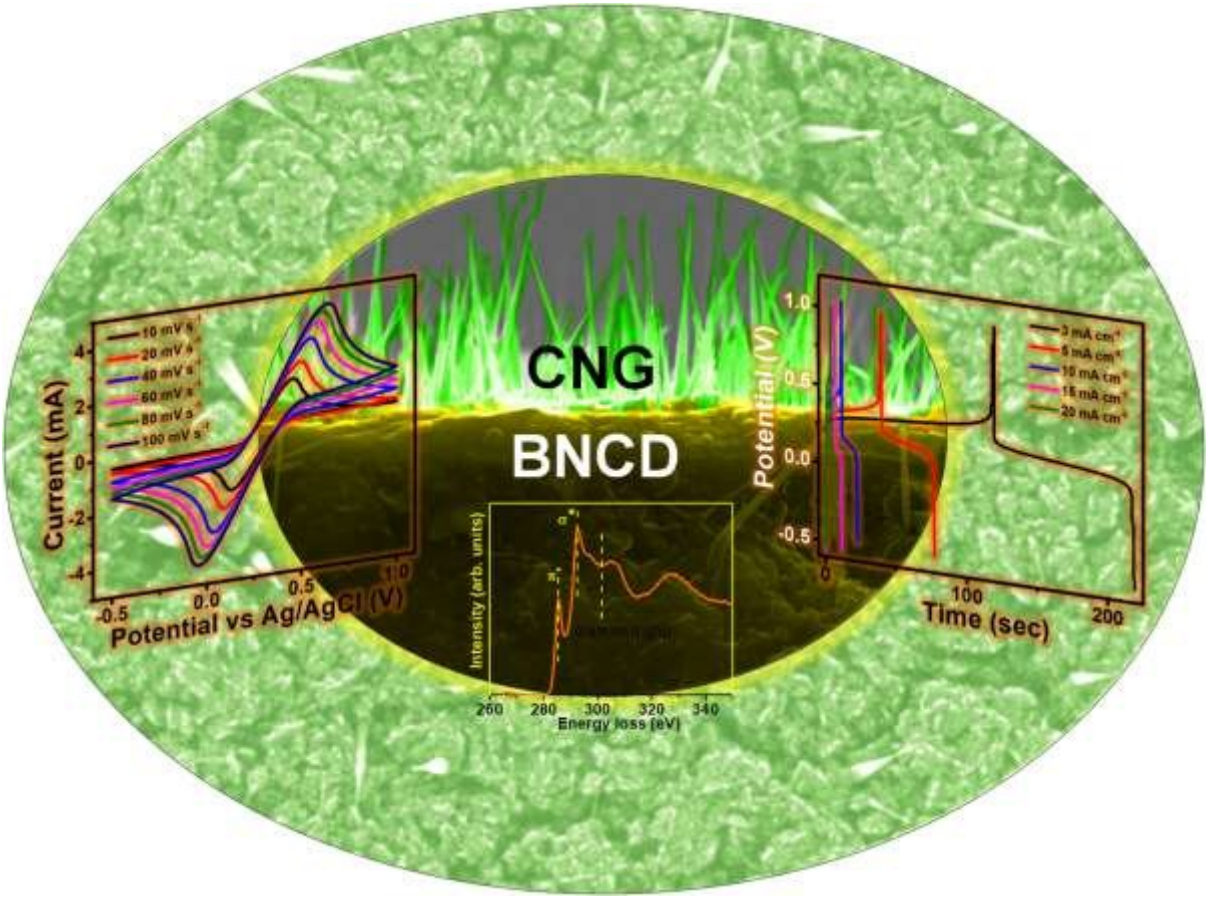

Boron doped nanocrystalline diamond-carbon nanograss hybrid as an efficient supercapacitor electrode